ADVANCING EARTH AND SPACE SCIENCES

JGR Atmospheres

RESEARCH ARTICLE

10.1029/2025JD044592

Diurnal Cycle and Seasonality of Cirrus Clouds Over the Amazon From a Seven-Year Ground-Based Lidar Record

Luan P. Cordeiro[1], **Diego A. Gouveia**[2], **and Henrique M. J. Barbosa**[3]

[1]Physics Institute, University of São Paulo, São Paulo, Brazil, [2]Royal Netherlands Meteorological Institute (KNMI), De Bilt, The Netherlands, [3]Department of Physics, University of Maryland Baltimore County, Baltimore, MD, USA

Key Points:

- Cirrus cover and optical depth follow a strong diurnal cycle with a noon minimum and a convection-driven late afternoon maximum
- Cirrus clouds stand higher and are thicker in the wet season, whereas lidar ratios peak in the dry season, revealing important seasonality

Supporting Information:

Supporting Information may be found in the online version of this article.

Correspondence to:

H. M. J. Barbosa and L. P. Cordeiro,
hbarbosa@umbc.edu;
luancordeiro@usp.br

Citation:

Cordeiro, L. P., Gouveia, D. A., & Barbosa, H. M. J. (2025). Diurnal cycle and seasonality of cirrus clouds over the Amazon from a seven-year ground-based lidar record. *Journal of Geophysical Research: Atmospheres*, *130*, e2025JD044592. https://doi.org/10.1029/2025JD044592

Received 12 JUN 2025
Accepted 22 OCT 2025

Author Contributions:

Conceptualization: Henrique M. J. Barbosa
Data curation: Henrique M. J. Barbosa
Formal analysis: Luan P. Cordeiro
Investigation: Luan P. Cordeiro, Diego A. Gouveia, Henrique M. J. Barbosa
Methodology: Diego A. Gouveia
Software: Luan P. Cordeiro, Diego A. Gouveia
Supervision: Henrique M. J. Barbosa
Visualization: Luan P. Cordeiro
Writing – original draft: Luan P. Cordeiro
Writing – review & editing: Luan P. Cordeiro, Diego A. Gouveia, Henrique M. J. Barbosa

Abstract Cirrus clouds strongly influence Earth's radiation balance, yet their optical properties and formation pathways add uncertainty to climate models. Satellites offer a global view of cirrus but have key limitations: passive sensors struggle to detect thin layers, and active instruments in polar orbits miss the diurnal cycle. Long-term records of ground-based lidar measurements can help fill this important observational gap. Here, we analyzed 5 481 h of lidar data gathered near Manaus, Brazil (July 2011–December 2017), to characterize the cirrus clouds over the Amazon rainforest. An automated routine set cloud boundaries, and multiple-scattering-corrected retrievals yielded cloud optical depth (COD) and the lidar ratio. Cirrus were found to occur with a frequency of 73.1%. Thin layers (COD = 0.03-0.30) are the most prevalent with a 48.4% relative frequency, followed by opaque (>0.30; 26.4%) and subvisual (<0.03; 25.2%). The mean base and top altitudes were 12.8 ± 2.2 km and 14.4 ± 1.9 km, and the lidar ratio averaged 26.1 ± 8.3 sr. Thinner clouds clustered near the tropopause, while higher tops tracked the tropopause variability. A clear diurnal cycle shows a noon minimum frequency of occurrence and a late-afternoon maximum, strongest for opaque cirrus and consistent with convective-anvil outflow. Optical properties such as COD, lidar ratio, and geometric properties follow a well-defined daily rhythm. Seasonally, cirrus are more frequent in the wet season (81.8%) than in the dry (56.7%). Bases, tops, and thickness are likewise larger in the wet season, whereas lidar ratios peak in the dry season. This long-term record benchmarks satellite retrievals, sharpens radiative impact calculations, and clarifies cirrus formation over tropical forests.

Plain Language Summary Cirrus clouds, which occur at high altitude and are composed of ice crystals, regulate Earth's energy balance by both trapping outgoing heat and reflecting incoming sunlight. To improve climate models, we need reliable statistics on where cirrus occur, when they form, and how optically thick they are. To address this need, we operated a ground-based lidar above the Amazon rainforest, 20 km north of Manaus, for seven years (2011–2017). In 5481 hr of data, we spotted cirrus in roughly three-quarters of all five-minute snapshots—rising to more than four-fifths during the wet season. These ice clouds followed a clear daily rhythm: they were rarest around local noon, then increased after afternoon thunderstorms (13:00–15:00 LT), and peaked late in the afternoon. Most layers were "thin" or even "sub-visible." On average, their bases sat 12.8 km above sea level and their tops 14.4 km, climbing higher and growing thicker during the wet season. By documenting the observed frequency, thickness, and timing of Amazonian cirrus, these new statistics enable climate researchers to better constrain their models so that the clouds' interaction with incoming and outgoing radiation—and therefore their warming or cooling effect—is simulated far more accurately.

1. Introduction

Globally, clouds cover approximately 67% of the Earth's surface (King et al., 2013). Cirrus clouds account for 16.7% of this coverage, with a significant portion found in tropical regions, where their frequency of occurrence reaches approximately 56% (Sassen et al., 2008). This frequency is even higher in the Amazon, reaching 88% (Gouveia et al., 2017). Cirrus clouds are composed entirely of ice crystals and are the most common type of high-altitude cloud. They exhibit an extensive horizontal spread but have smaller vertical dimensions and are typically found at altitudes between 6 and 18 km (Sassen et al., 2008). Due to the strong winds at these altitudes, cirrus clouds often develop a characteristic filamentous appearance as ice crystals are advected. Moreover, they have low water content (10^{-4}–0.5 g m^{-3}) and while their cloud optical depth (COD) is not strictly less than 0.3, it generally remains below that threshold (Lohmann et al., 2016). These clouds can form from the detachment and dispersion of the anvil of deep convective clouds (Gouveia et al., 2017; Mace et al., 2006; McFarquhar et al., 2000; Sassen et al., 2009) or as a result of large-scale uplift, for instance, associated with fronts and gravity waves (Krämer et al., 2016; Potter & Holton, 1995).

On a global scale, Gasparini and Lohmann (2016) estimated that cirrus clouds contribute an average radiative forcing of 5.7 Wm^{-2} at the top of the atmosphere using a general circulation model. In the Amazon, these values are significantly higher, with radiative forcing estimated to be about 15.3 Wm^{-2} at the top of the atmosphere and -3.7 Wm^{-2} at the surface (Gouveia, 2018). This effect is greater than the radiative forcing from anthropogenic carbon dioxide emissions, highlighting the importance of understanding cirrus cloud properties. Consequently, over the past decades, extensive scientific efforts have been made to improve our knowledge of their properties (Comstock et al., 2002; Pandit et al., 2015; Sassen et al., 2008). However, studies of cirrus clouds in tropical forest regions remain limited (Gouveia et al., 2017).

Cirrus clouds remain a significant source of uncertainty in weather and climate models (Heymsfield et al., 2017; Liou, 1986; Lynch et al., 2002). Their representation is challenging because the mechanisms governing their formation are not yet fully understood, involving a competition between homogeneous and heterogeneous nucleation pathways influenced by aerosols and dynamics (Jeggle et al., 2025; Jensen et al., 2024; Kärcher et al., 2022; Lin et al., 2025; Luo et al., 2005). Furthermore, their radiative impact depends on both optical depth and cloud coverage, as well as the properties of the underlying surface, which studies have shown to strongly affect the high-cloud radiative effect (Gasparini et al., 2023; Horner & Gryspeerdt, 2025; Lynch et al., 2002). Therefore, detailed information on their frequency of occurrence and optical properties is crucial for improving and verifying climate model simulations (Atlas et al., 2024; Gasparini et al., 2023).

For this purpose, ground-based measurements (Comstock et al., 2002; Gouveia et al., 2017; Hoareau et al., 2013; Nakoudi et al., 2021; Pandit et al., 2015), in situ observations (Krämer et al., 2016; Krisna et al., 2018; Luebke et al., 2013; Spichtinger & Gierens, 2009), and satellite data (Portella & Barbosa, 2024; Sassen et al., 2008, 2009; Winker et al., 2010) have been used. Ground-based and satellite studies often rely on lidar (light detection and ranging). Lidar is an effective tool for studying cirrus clouds because it provides high-resolution measurements in both time and altitude. By transmitting laser pulses into the atmosphere and measuring the backscattered light, lidar can retrieve important optical properties such as optical depth and the depolarization ratio. This capability allows for detecting optically thin and subvisible cirrus clouds that may be overlooked by cloud radars or passive remote sensing methods (Haladay & Stephens, 2009). Satellite-borne lidars can provide global cirrus coverage, but often at limited observational times (Wehr et al., 2023; Winker et al., 2009). On the other hand, instruments on the ground can provide details on the temporal evolution and vertical structure of cirrus clouds but only at a single location (Giannakaki et al., 2007; Gouveia et al., 2017; Hoareau et al., 2013; Nakoudi et al., 2021).

This study examines the optical and geometric properties of cirrus clouds in the Amazon, investigating their diurnal and seasonal variability and exploring their formation mechanisms. The analysis is based on long-term lidar observations from the ACONVEX experimental site in Manaus, Brazil, operated by the Atmospheric Physics Laboratory at the University of São Paulo between 2011 and 2017. Using a cloud-detection algorithm, we demonstrate how cirrus thicken and expand horizontally in late-afternoon convective outflow and then thin and drift upward toward the tropopause overnight—a daily rhythm that weather and climate models must capture. We also find that cirrus appear more often and reach higher altitudes in the wet season; their lidar ratios also shift with the cloud type. Finally, a comparison with other tropical studies place these findings in a broader context and highlights the distinct behavior of Amazonian cirrus.

This paper is organized as follows: Section 2 describes the study site, data set, and methodology. Section 3 presents the results, including the cirrus frequency of occurrence, their optical and geometric properties, and seasonal and diurnal trends. Section 4 discusses the key findings, comparing them with previous studies and exploring their broader implications. Finally, Section 5 summarizes the main conclusions and suggests directions for future research.

2. Data and Methods

2.1. Experimental Site

The observations used in this study were conducted at the ACONVEX (Aerosols, Clouds, cONVection EXperiment) site (Barbosa et al., 2014), also known as T0e in the nomenclature of the GoAmazon2014/15 experiment (Martin et al., 2016). It is located in the central Amazon region, within the Embrapa Amazônia Oriental campus, 20 km north of Manaus, Brazil (2.89°S, 59.97°W) at an altitude of 100 m a.s.l. in a region of pristine rainforest. Established by the Atmospheric Physics Laboratory (LFA) of the University of São Paulo (USP) in 2011, the site was operated continuously until 2017 (see Figure S1 in Supporting Information S1 for the site location).

The Amazon rainforest, characterized by its tropical humid climate, has a distinct precipitation pattern. The wet season typically spans from January to April, the dry season from June to September, and transitional months occur in between (Machado et al., 2014). Convection happens throughout the year, but its intensity varies with the seasonal migration of the intertropical convergence zone. Deep convective activity is pronounced during the wet season and diminishes as the convergence zone shifts northward during the dry season.

2.2. Instrumentation

Central to this study is the UV Raman lidar system (LR-102-U-400/HP, manufactured by Raymetrics Advanced Lidar Systems), which operated at ACONVEX from July 2011 to December 2017. This instrument measures the elastic backscatter at 355 nm and Raman scattering at 387 nm (nitrogen) and 408 nm (water vapor). Return signals are measured in analog (elastic, N_2) and photon-counting (elastic, N_2, H_2O) modes. The weak Raman signals can only be detected at night due to the solar background during the day. Hence, this study uses the photon-counting elastic return signal only. This lidar operates in an automated mode and is tilted 5° from the zenith to minimize reflections from horizontally oriented ice crystals. Measurements were conducted daily, except around the solar maximum (12:00 local time, UTC-4). Further details about the instrumentation are available in Barbosa et al. (2014). Early analyses demonstrated the instrument's reliability, including consistent aerosol optical depth retrievals compared to AERONET measurements (Barbosa et al., 2014) and retrieval of cirrus optical properties (Gouveia et al., 2014).

2.3. Data Set

The data set used in this study spans from July 2011 to December 2017, with lidar measurements averaged into 5-min intervals with a 7.5-m vertical resolution, resulting in a total of 220,400 profiles. Of these, 65,774 profiles (∼30%), corresponding to approximately 5,481 hr of observation, were classified as having a good signal-to-noise ratio (SNR) at cirrus altitudes and were included in the analysis. Following the criteria established by Gouveia et al. (2017), a lidar profile is considered to have a good SNR if it has a molecular signal with $\mathrm{SNR}(z = 16\,\mathrm{km}) > 1$ or could have satisfied this condition if the cirrus clouds themselves had not attenuated it. These conditions ensure that optically thin cirrus clouds are detectable during the day and night in profiles with good SNR (see Section 2.4). Generally, a good SNR is achieved when the profile is not obscured by liquid or mixed-phase clouds or strongly attenuated by fog or precipitation. Figure S2 in Supporting Information S1 shows the availability of data throughout the study period. The number of good SNR profiles varies from 1,225 in January to 9,802 in August. Regarding the hour of the day, there are fewer profiles with good SNR during the daytime (about 495 at 10:00 LT and 265 at 14:00 LT) but still enough to achieve statistical significance.

Radiosonde data provide temperature and pressure profiles necessary for inverting lidar signals. They are launched twice daily (00:00 and 12:00 UTC) from the Ponta Pelada airport in Manaus (3.14°S, 59.98°W, WMO code 82332), approximately 28.5 km south of the measurement site (see Figure S1 in Supporting Information S1).

Precipitation data were obtained from the Climate Prediction Center morphing technique (CMORPH) data set (Xie et al., 2017), covering the same period as the lidar measurements. CMORPH provides global precipitation estimates at a spatial resolution of 8 km × 8 km and a temporal resolution of 30 min. CMORPH combines passive microwave measurements from low-Earth orbit satellites and adjusts for biases using calibration analyses with surface observations and data from the Global Precipitation Climatology Project (GPCP). For our analysis, the precipitation rate is averaged over an area of ±5° latitude and longitude centered on the Embrapa campus and from 2011 to 2017.

The tropopause height was determined using data from NASA's atmospheric infrared sounder (AIRS) aboard the Aqua satellite. Tropopause heights were extracted from the AIRS Level 3 Monthly Gridded Retrieval Product, Version 7, which provides global coverage with a spatial resolution of 1° × 1°. The tropopause height was averaged over a region of ±5° latitude and longitude centered at the study site.

2.4. Identification of Cirrus Layers

The cloud detection algorithm developed by Gouveia et al. (2014) was used to identify the base and the top of cloud layers. The detection strategy assumes that in a clear atmosphere, the lidar signal decreases monotonically with altitude. When a cloud is present, the signal increases significantly, and these positive variations are identified as potential cloud bases. If the signal rises over three standard deviations above the mean value for a clear atmosphere, the altitude is defined as the legitimate cloud base. The cloud top is where the signal returns to the below cloud base value, with a slope consistent with a clear atmosphere. More details can be found in Gouveia et al. (2014).

A lidar signal can be fully attenuated within dense cloud layers, making it impossible to determine the cloud top. To evaluate whether the detected top is genuine, a *t* test with a 10% significance level was conducted. The signal immediately above the detected top is compared to the background noise. The detected top is classified as an apparent cloud top if no statistically significant difference is found. Profiles with apparent tops were excluded from our analysis. Effectively, this introduces a maximum threshold for the cirrus optical depth of about ∼3.0 (see Figure 1g).

The algorithm is applied to the portion of the profile above 5 km. Following a similar methodology described by Seifert et al. (2007); Campbell et al. (2015), cirrus clouds are considered isolated layers with bases above 8 km and cloud top temperatures lower than −37°C. Two cloud layers are considered independent if separated by at least 500 m.

The uncertainties associated with cloud identification using this algorithm were evaluated by Gouveia (2018) through Monte Carlo simulations. Their results showed that the algorithm detects 99% of clouds with COD greater than 0.005 and a particle backscatter coefficient greater than $1\ \mathrm{Mm}^{-1}\mathrm{sr}^{-1}$ for lidar signals with a molecular $\mathrm{SNR}(z = 16\ \mathrm{km}) > 1$ (see Section 2.3 for details). It is important to note that this is not the SNR inside the cloud, which typically ranges from 6 to 36 for cirrus layers detected by our instrument.

2.5. Transmittance Method and Multiple Scattering Correction

We used the transmittance method to retrieve cirrus optical properties from lidar signals measured just above and below the cloud (Young, 1995). By comparing these signals, we determined the cloud's optical depth, which constrained the extinction profile retrieved through the Klett inversion (Klett, 1985), thus allowing the simultaneous estimation of the lidar ratio (LR). The transmittance method converges well when the COD is sufficiently large (τ above 0.03). In 26.7% of the retrievals, where convergence was not achieved, the mean LR of 25 sr was applied based on the literature survey summarized in Table 3. This is necessary to estimate the layer COD; however, these LR values are not included in the statistical analyses.

The inversion of elastic lidar signals using the Klett method assumes that a photon undergoes only a single scattering event. However, multiple scattering may significantly influence cirrus cloud measurements, wherein photons undergo numerous scattering events before being detected. This effect boosts the backscattered signal and leads to underestimates in the retrieved extinction coefficient (Wandinger, 1998).

To account for and correct the effects of multiple scattering on our retrievals, we use an interactive approach described in Gouveia et al. (2017). It relies on the forward model proposed by Hogan (2008), which simulates single and multiple-scattering signals based mainly on the extinction coefficient profile, the effective ice particle size, and the receiver field of view. For the multiple scattering model, we used a temperature-dependent parameterization of the ice crystals' effective radius based on a climatology of aircraft measurements of tropical cirrus data (Krämer et al., 2016). This parametrization includes observations over the Amazon region in 2014 with the German aircraft HALO (Wendisch et al., 2016).

2.6. Statistical Analysis

We conduct statistical analysis for cloud base and top altitudes, cloud geometric thickness, COD, LR, and the frequency of occurrence of cirrus clouds. The frequency of occurrence is calculated as the number of profiles with at least one cirrus layer divided by the number of good profiles. The data set is separated into three distinct seasons: wet (January to April), dry (June to September), and transition (spanning May and October to December) based on Machado et al. (2014). Additionally, the analysis is categorized by COD, with results presented for

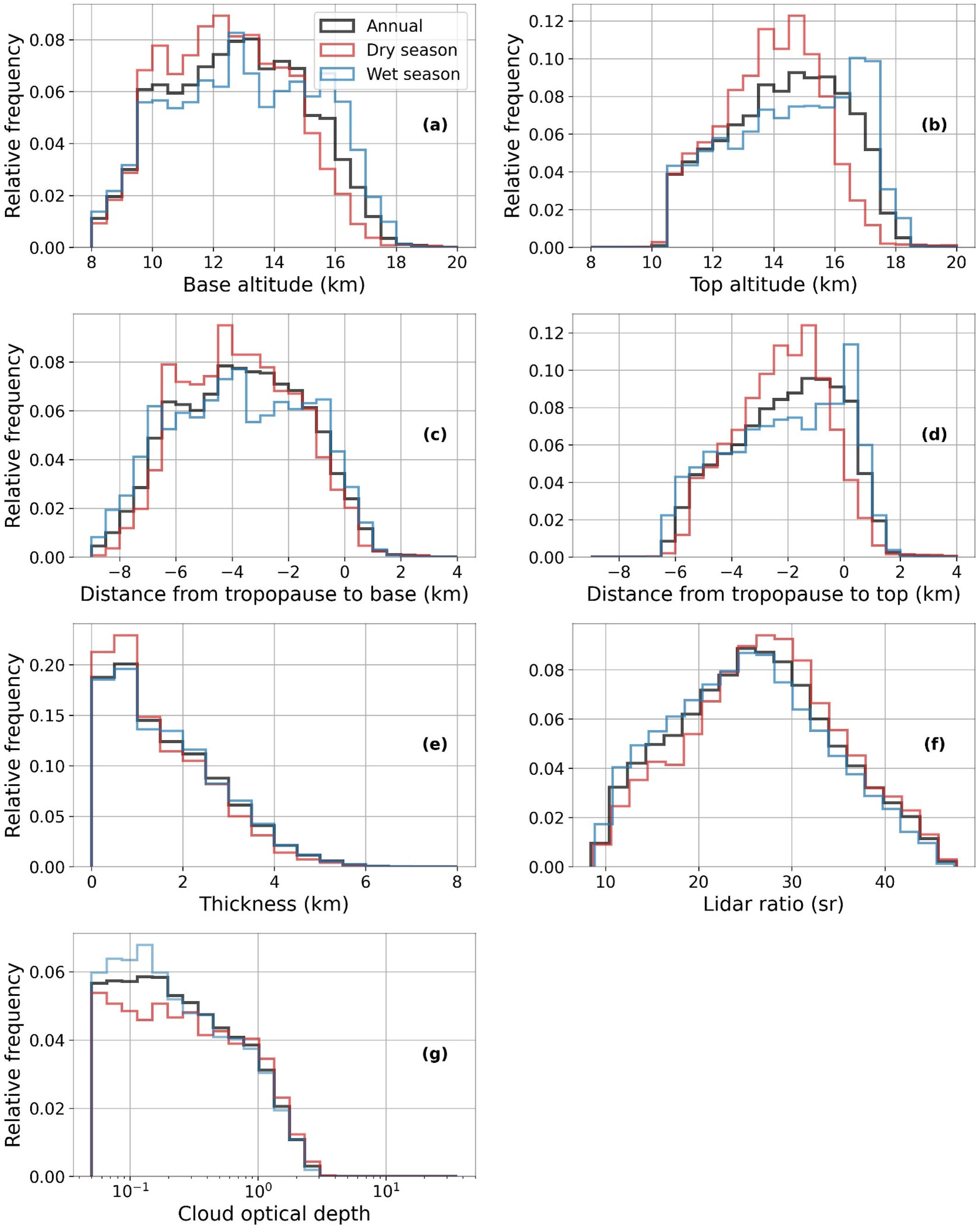

Figure 1. Normalized histograms depicting the distribution of (a) base altitude, (b) top altitude, (c) distance from the tropopause to the base, (d) distance from the tropopause to the top, (e) thickness, (f) LR, and (g) COD. The black curve represents data from the entire measurement period, while the blue and red curves correspond to the wet and dry seasons, respectively.

subvisual clouds ($COD < 0.03$), thin clouds ($0.03 \leq COD < 0.3$), and opaque clouds ($COD > 0.3$) based on Sassen and Cho (1992). The frequency of occurrence of the different categories is obtained by counting the number of profiles with at least one cirrus layer of a particular category. Finally, the uncertainty in the frequency of occurrence is estimated from the binomial distribution.

For profiles with a good SNR, identifying the presence of cirrus clouds is straightforward, and the probability of detection can be reliably assessed based on the COD (Gouveia, 2018). However, when the signal is weak or

Table 1

Statistical Summary of Column-Integrated Cirrus Properties for the Total Observation Period, as Well as the Wet, Transition, and Dry Seasons

	Total	Wet	Transition	Dry
No. prof. measured	220,400	60,730	91,758	67,912
No. prof. analyzed	65,774	12,353	21,487	31,934
No. prof. discarded, low SNR	154,023	48,214	69,974	35,835
No. prof. discarded, apparent top	603	163	297	143
No. prof. with cirrus	47,850	10,561	18,410	18,879
Frequency of occurrence (%)	73.1	81.8	80.8	56.7
Frequency of opaque profiles (%)	22.6	29.4	26.4	13.6
Frequency of thin profiles (%)	34.1	38.2	39.8	24.9
Frequency of SVC profiles (%)	16.5	14.2	14.7	18.2
Column-integrated COD	0.37 (0.49)	0.39 (0.39)	0.39 (0.39)	0.35 (0.35)
No. of cirrus layers per cloud prof.	1.4 (0.61)	1.51 (0.68)	1.47 (0.63)	1.28 (0.51)

Note. The frequency of occurrence was calculated using the conditional sampling technique as the ratio of the number of profiles with cirrus to the number of profiles with good SNR. The column-integrated COD is used to distinguish between opaque, thin, and SVC profiles and compute their frequencies. Numbers in parentheses are the sample standard deviation. Profiles from 10:30 to 13:30 LT are not included in the analysis.

entirely attenuated, it becomes challenging to confidently detect the presence of clouds. This creates difficulties in assessing the frequency of occurrence of cirrus clouds from ground-based lidar measurements, particularly in regions like the Amazon, where low clouds are prevalent. As a result, profiles with a good SNR are more frequent during the dry season and at night, as already discussed, which introduces potential biases (see Figure S2 in Supporting Information S1).

To mitigate these sampling biases arising from data distribution differences, we adopted a conditional sampling approach for computing the frequency of occurrence, following the methodology described by Gouveia et al. (2017), who drew on the work of Thorsen et al. (2011) and Protat et al. (2014). This approach assumes the independence of high clouds from the presence of artifacts that degrade the lidar signal. These could be low clouds, fog, precipitation, or thick aerosol layers. The frequency of occurrence is calculated for each hour across 24 hr, resulting in a diurnal cycle. To estimate the monthly frequency, we average these diurnal cycles across the month. The seasonal frequency is derived by averaging the monthly frequencies within a given season. The annual frequency of occurrence is then determined by averaging the seasonal frequencies.

In contrast to Gouveia et al. (2017), our study accounts for the degradation of the SNR due to sunlight interference. Subvisual cirrus (SVC) clouds, detectable at night, may go unnoticed during the day due to the reduced sensitivity of the lidar under daylight conditions. To minimize any bias arising from the enhanced detection of clouds at night, only layers with a COD greater than 0.005 were considered. According to simulations by Gouveia (2018), cirrus clouds with a COD above this threshold can be reliably detected day and night. Therefore, this minimum threshold ensures uniform detectability in daytime and nighttime conditions, minimizing potential biases in the derived cirrus properties. Although this threshold excludes the thinnest SVC cirrus (≈8% of cases), it provides consistent and comparable statistics for properties such as base height, top height, thickness, and COD.

3. Results

3.1. Average Optical and Geometric Properties

We start by investigating the overall properties of the cirrus clouds. Table 1 provides a statistical summary of the 5-min lidar profiles measured from July 2011 to December 2017. During this period, cirrus clouds were present in 73.1% of the profiles, exhibiting marked seasonality: occurrence peaked at 81.8% in the wet season and decreased to approximately 56.7% in the dry season. On average, each cirrus-containing profile featured 1.40 cirrus layers, with a column-integrated COD of 0.37. Concerning cloud categories, profiles with thin cirrus (34.1%) were most frequent, followed by opaque (22.6%) and SVC (16.5%). The occurrence frequency of thin and opaque categories

Table 2
Statistical Summary Based on Cirrus Layers for the Total Observation Period, as Well as the Wet, Transition, and dry Seasons

	Total	Wet	Transition	Dry
All layers				
No. of layers	65,456	15,455	26,246	23,755
Base height (km)	12.8 (2.2)	13.1 (2.3)	13.0 (2.2)	12.5 (2.0)
Top height (km)	14.4 (1.9)	14.7 (2.0)	14.7 (1.9)	13.9 (1.6)
Thickness (km)	1.61 (1.17)	1.62 (1.16)	1.73 (1.22)	1.46 (1.10)
Lidar ratio (sr)	26.1 (8.3)	25.3 (8.3)	25.5 (8.4)	27.1 (8.1)
Cloud optical depth	0.27 (0.40)	0.26 (0.39)	0.27 (0.39)	0.28 (0.43)
Base above tropopause (%)	4.0	4.7	4.7	2.9
Top above tropopause (%)	15.4	20.3	19.7	7.4
Relative frequency of opaque cirrus (%)	26.4	25.5	26.9	26.5
Relative frequency of thin cirrus (%)	48.4	51.7	51.1	43.0
Relative frequency of SVC (%)	25.2	22.9	22.0	30.5
Opaque layers				
No. of layers	17,310	3,934	7,063	6,313
Base height (km)	10.9 (1.6)	11.0 (1.7)	11.1 (1.7)	10.7 (1.4)
Top height (km)	13.8 (1.7)	13.8 (1.8)	14.0 (1.8)	13.4 (1.5)
Thickness (km)	2.82 (1.05)	2.83 (1.03)	2.95 (1.08)	2.67 (1.00)
Lidar ratio (sr)	28.8 (6.9)	28.7 (7.2)	28.6 (7.3)	29.0 (6.3)
Cloud optical depth	0.80 (0.47)	0.8 (0.46)	0.76 (0.45)	0.84 (0.50)
Frequency of occurrence (%)	21.6	26.8	24.2	13.9
Thin layers				
No. of layers	31,582	7,983	13,416	10,183
Base height (km)	13.1 (1.9)	13.5 (2.0)	13.3 (1.9)	12.6 (1.6)
Top height (km)	14.6 (1.9)	15.0 (2.0)	14.9 (1.9)	14.0 (1.6)
Thickness (km)	1.48 (0.88)	1.49 (0.89)	1.57 (0.92)	1.34 (0.79)
Lidar ratio (sr)	24.7 (8.9)	23.3 (8.4)	23.7 (8.7)	26.6 (9.2)
Cloud optical depth	0.12 (0.07)	0.11 (0.07)	0.12 (0.07)	0.11 (0.07)
Frequency of occurrence (%)	40.6	47.4	48.1	26.5
SVC layers				
No. of layers	16,564	3,538	5,767	7,259
Base height (km)	14.1 (1.9)	14.5 (2.1)	14.4 (1.9)	13.8 (1.7)
Top height (km)	14.7 (1.9)	15.0 (2.1)	15.0 (1.9)	14.4 (1.7)
Thickness (km)	0.59 (0.39)	0.56 (0.37)	0.61 (0.43)	0.59 (0.37)
Lidar ratio (sr)	22.2 (7.2)	21.3 (6.8)	22.1 (7.4)	22.7 (7.2)
Cloud optical depth	0.016 (0.007)	0.016 (0.007)	0.016 (0.007)	0.015 (0.007)
Frequency of occurrence (%)	22.1	22.2	22.4	21.5

Note. The frequency of occurrence of opaque layers is the probability of finding at least one opaque layer in the profile, and the same holds for thin and SVC layers. The average optical and geometric properties are given for each period and optical depth category, along with the sample standard deviation in parentheses.

decreases during the dry season, whereas the frequency of SVC increases. Considering all cirrus layers, thin layers are the most frequent (48.4% of the total number of layers observed), followed by opaque (26.4%) and SVC (25.2%) (Table 2).

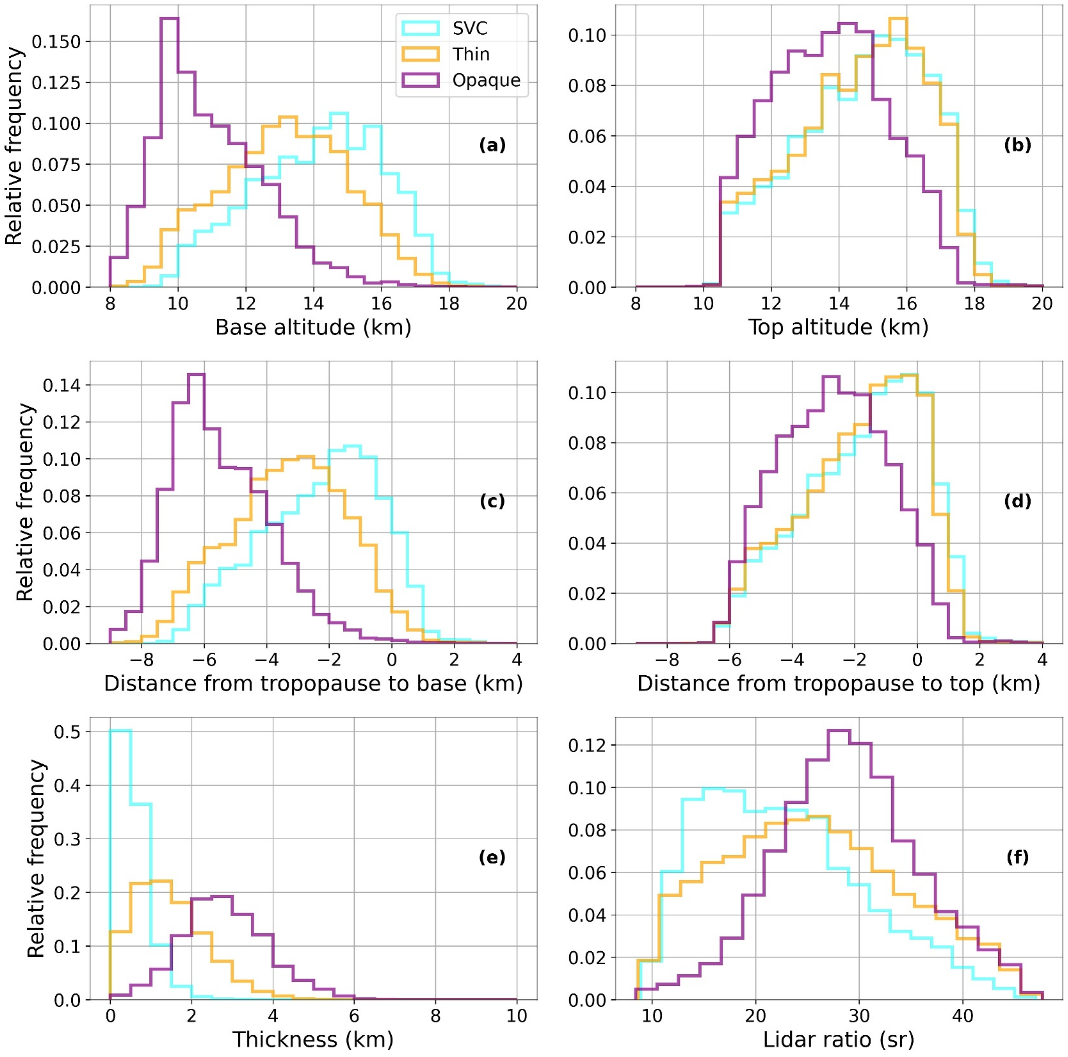

Figure 2. Normalized histograms depicting the distribution of (a) base altitude, (b) top altitude, (c) distance from the tropopause to the base, (d) distance from the tropopause to the top, (e) thickness, and (f) LR. The purple, orange, and cyan curves correspond to opaque, thin, and SVC cirrus, respectively.

The distribution of optical and geometric properties of each cirrus layer is influenced more strongly by the cirrus cloud category than by seasonal changes. Figure 1 presents histograms of these properties stratified by season, while Figure 2 shows them segregated by cirrus category. Table 2 further summarizes these properties for each season and cloud category, providing means and standard deviations.

Cirrus clouds occur at higher altitudes during the wet and transition seasons than in the dry season, while optically thinner cirrus occur at higher altitudes than thicker cirrus. Figures 1a and 1b reveal that cirrus cloud bases and tops reach higher altitudes in the wet seasons than the dry season. Also, the base and top altitudes of opaque clouds are lower than those of thin cirrus and SVC (see Figures 2a and 2b). Although the top altitude distributions of thin cirrus and SVC are similar, the base altitude of thin cirrus is lower than that of SVC. Consistent with these histograms, Table 2 reports that, on average, SVC base altitudes exceed those of the other two categories by at least 1 km.

The probability of finding cirrus cloud bases and tops above the tropopause is higher during the wet season than the dry season. Figures 1c and 1d present the distributions of the distance from the tropopause to the cirrus cloud base and the top, respectively. We observe a small fraction of cirrus clouds with bases above the tropopause in both seasons, but they appear more frequently during the wet season. Figure 2c indicates that thin cirrus and SVC

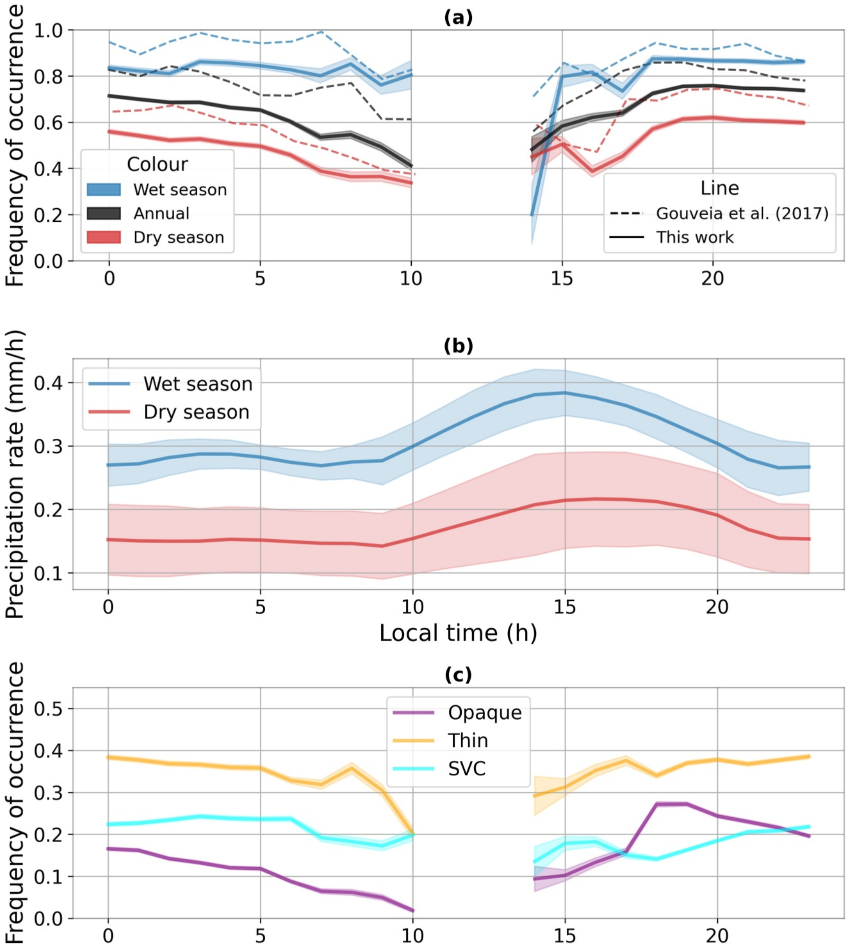

Figure 3. Diurnal cycle of (a) cirrus occurrence frequency for annual, wet, and dry periods, (b) satellite-based precipitation rate, and (c) occurrence frequency for opaque, thin, and SVC layers. The continuous curves represent the results from this study, while the dashed curves correspond to those reported by Gouveia et al. (2017). Shaded areas indicate the uncertainty, either from the binomial distribution (frequency) or the standard deviation of the mean (precipitation). Values are calculated for 1-hr intervals, centered on each full hour.

clouds can extend their bases into the tropopause layer/lower stratosphere, whereas opaque cirrus remain confined below the tropopause. In Figure 1d, the mode of the distribution of cirrus tops is located at the tropopause during the wet season, whereas during the dry season, the mode is approximately 1.5 km below the tropopause. Hence, the clutter of cirrus clouds at the tropopause is mainly due to thin cirrus and SVC, as seen in Figure 2d.

Figures 1e and 1g illustrate that COD and geometric thickness exhibit low seasonality. However, Table 2 reports that cirrus clouds tend to be geometrically thicker during the wet and transition seasons than the dry season. Moreover, optically thicker clouds also tend to be geometrically thicker (Figure 2e).

The LR is another important optical property displaying categorical variability but little seasonality (compare Figures 1f and 2f). It varies from 25.3 sr (wet) to 27.1 sr (dry), which is only about 6.9% of the annual mean value. In contrast, it varies from 22.2 sr (SVC) to 28.8 sr (opaque), which is more than 25% of the mean. Table 2 quantifies these LR differences by season and the cirrus type.

3.2. Diurnal Cycle

We now investigate the diurnal cycle of cirrus properties. First, we present seasonal differences in the diurnal cycle. The frequency of occurrence and most cirrus properties exhibit a well-defined diurnal cycle, which correlates with regional precipitation.

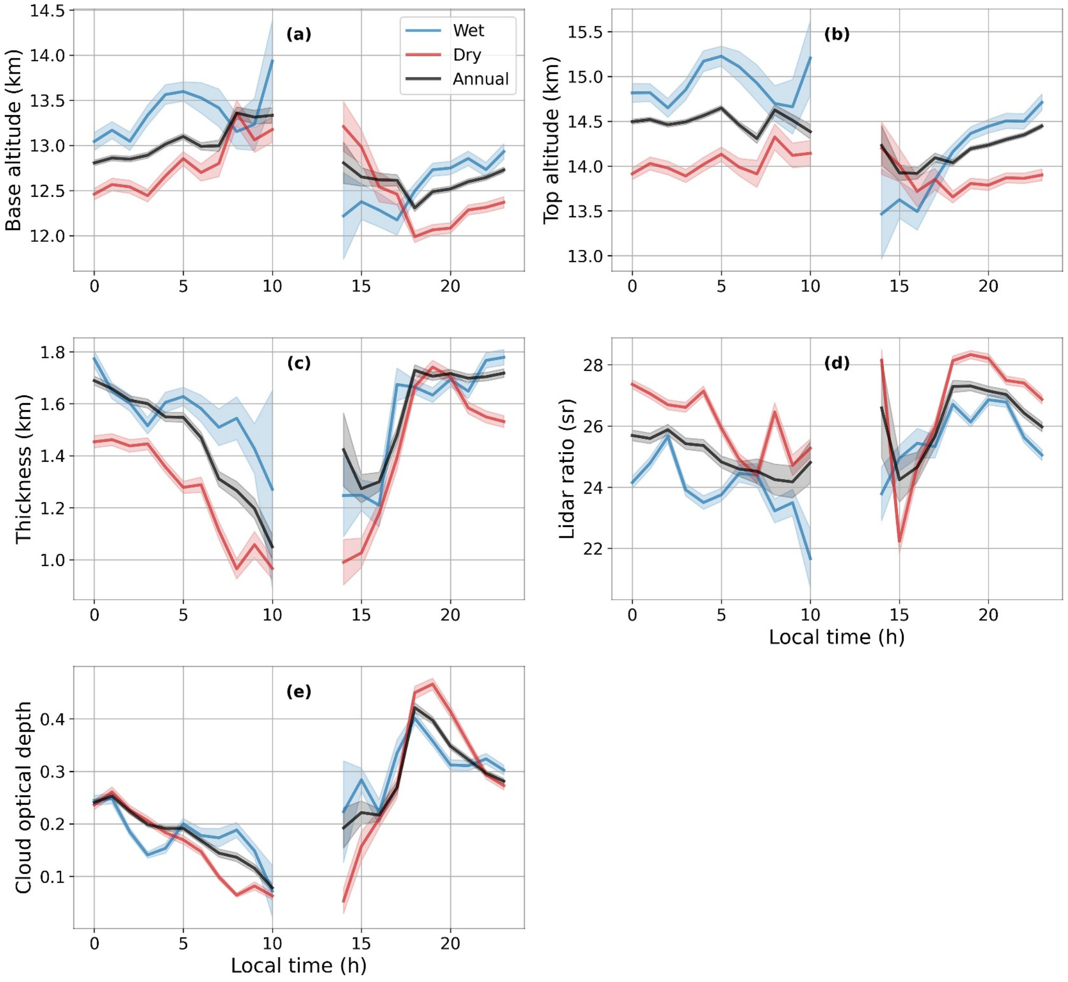

Figure 4. Diurnal cycle of mean (a) base altitude, (b) top altitude, (c) geometric thickness, (d) LR, and (e) COD categorized by seasons. Shaded areas indicate the uncertainty, as the standard deviation of the mean. Values are calculated for 1-hr intervals, centered on each full hour.

Figure 3a reveals that the frequency of occurrence is minimum around noon LT and increases in the afternoon. Maximum frequencies are found in late afternoon and early evening and gradually decline until the next sunrise. This pattern is consistent with previous work at the same site by Gouveia et al. (2017), who used only 1 year of data (shown as dashed lines). Figure 3b shows that precipitation peaks in the afternoon, particularly during the wet season and then tapers off at night and into the early morning. This timing highlights the correlation between convective processes and cirrus formation in this region: the development of convective systems during the afternoon is in phase with the occurrence of cirrus clouds. Additionally, the higher (lower) precipitation during the wet (dry) season is accompanied by a greater (smaller) presence of cirrus clouds.

Figure 4 displays the diurnal cycles of cirrus optical and geometric properties, organized by season. The diurnal cycle of cirrus clouds' base and top heights reaches a minimum in the afternoon (base at 12.3 km around 18:00 LT and top at 13.9 km around 15:00 LT) and increases through the evening. However, the top height tends to stabilize during the night, reaching about 14.5 km near midnight, while the base height rises into the early morning, peaking near 08:00 LT approximately 1.1 km above its afternoon minimum (Figures 4a and 4b). Both heights then begin to decrease again the following afternoon. The minimum of base and top heights occurs earlier in the wet season than in the dry season, and the subsequent increase during the afternoon also develops more rapidly in the wet season. Notably, between about 05:00 and 10:00 LT during the wet season, the top and base altitudes oscillate while cirrus thickness decreases (Figure 4c).

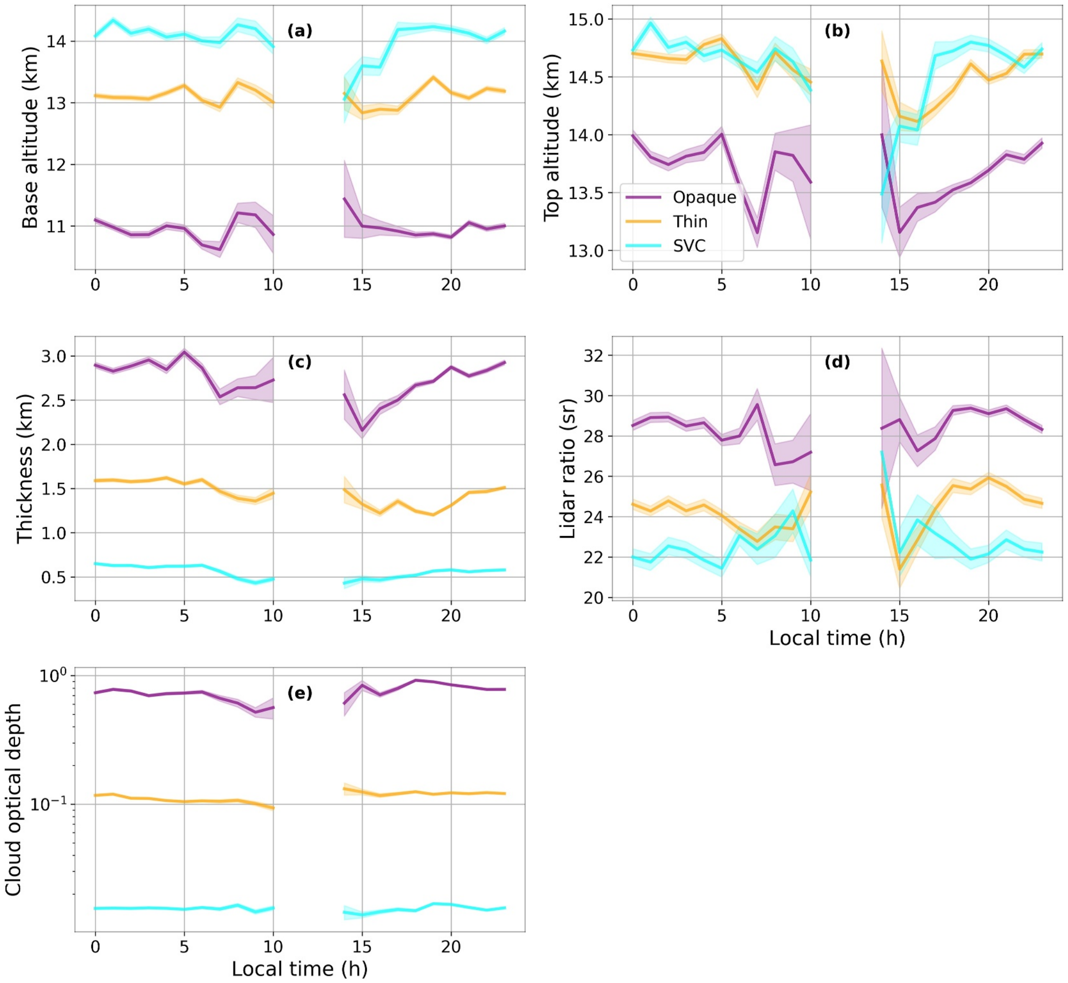

Figure 5. Diurnal cycle of mean (a) base altitude, (b) top altitude, (c) geometric thickness, (d) LR, and (e) COD, categorized by the optical depth of the layer. Shaded areas indicate the uncertainty, as the standard deviation of the mean. Values are calculated for 1-hr intervals, centered on each full hour.

As seen in Figure 4d, the LR follows a distinct diurnal cycle, reaching a minimum of 24 sr around 09:00 LT, peaking at approximately 27.3 sr at 18:00 LT and then decreasing through the night and early morning before rising again in the afternoon of the next day. This pattern is consistent across both the dry and wet seasons, though the LR is generally higher during the dry season.

Cirrus thickness peaks around 18:00 LT at 1.7 km, after reaching a minimum of 1.1 km near 10:00 LT (Figure 4c). It remains elevated into the evening and then decreases gradually during the night and early morning. A similar trend appears for the COD in Figure 4e, with a minimum of 0.09 near 10:00 LT and a maximum of 0.42 around 18:00 LT. Cirrus thinning proceeds earlier during the dry season than during the wet season.

We now discuss the diurnal cycle of cirrus properties segregated by the cloud type. As illustrated in Figure 3c, the afternoon rise in the presence of cirrus clouds is primarily driven by an increase in opaque and thin cirrus. The frequency of opaque cirrus starts to decrease around 18:00 LT, a few hours after the precipitation maximum. In contrast, the frequency of thin cirrus continues to increase until midnight before it starts to decrease. For SVC, the frequency peaks at 03:00 LT and starts to decrease after sunrise.

Figure 5 displays the diurnal cycles of cirrus optical and geometric properties, organized by the cirrus category. The diurnal cycle is generally more pronounced when the data are stratified by season than by cloud category. The base height remains relatively constant throughout the day (Figure 5a). For opaque (thin) cirrus, the top height reaches a minimum of 13.2 km (14.1 km) around 15:00 LT, increases through the afternoon, and then stabilizes

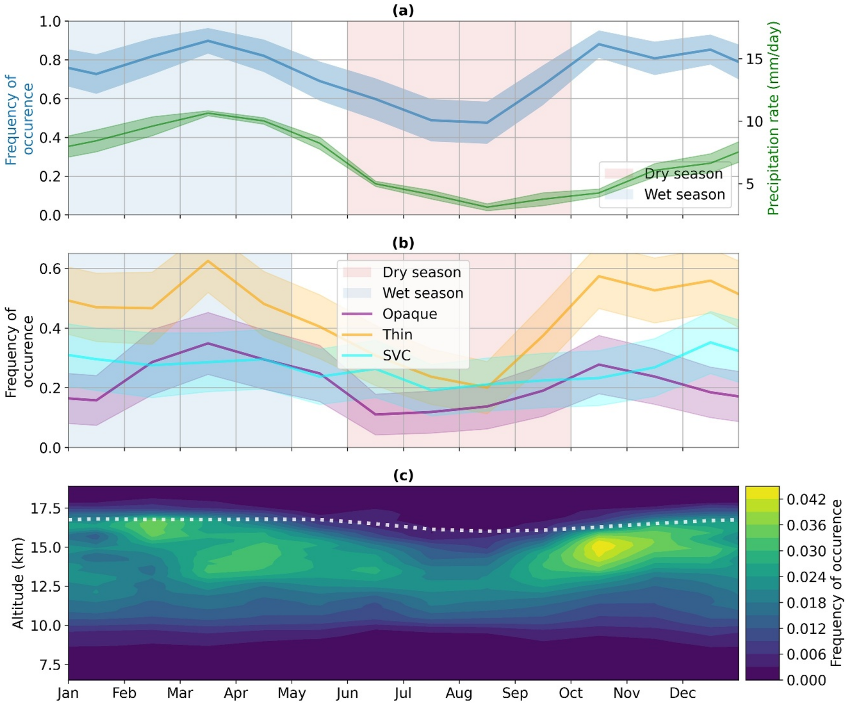

Figure 6. Seasonal cycle of (a) cirrus frequency of occurrence and the precipitation rate and (b) frequency of occurrence for opaque, thin, and SVC layers. Shaded areas indicate the uncertainty, either from the binomial distribution (frequency) or the standard deviation of the mean (precipitation). (c) Seasonal cycle of the probability of finding a cirrus at different altitudes. The sum of values across altitudes corresponds to the frequency of occurrence shown in panel (a). The white dotted curve represents the tropopause height.

near 13.9 km (14.7 km) around 23:00 LT before decreasing in the early morning (Figure 5b). In contrast, SVC shows a rapid increase in both base top altitude, of about 1 km, from 14:00 to 17:00.

Figures 5c and 5e report only minor variations in thickness and COD within each cirrus category. In general, cirrus tends to thicken during the afternoon and thin after sunrise, with the largest thickness variations observed in opaque clouds (from 2.2 to 3.0 km). As expected, the effects on the COD are smaller, as it is used to classify the cirrus into different categories. The exception is the COD of opaque cirrus, which clearly decreases after sunrise.

The diurnal variations of the lidar ratio segregated by cirrus category do not show a clear picture (Figure 5d). Thin and opaque cirrus seem to exhibit a minimum around 15:00 LT, rising through the afternoon to peak at about 20:00 LT and then declining overnight and into the early morning. In contrast, the SVC lidar ratio seems to peak at 14:00 LT. However, the decrease in SNR around noon affects the LR retrieval, especially for SVC layers, limiting the interpretation of its diurnal cycle variations.

3.3. Seasonal Cycle

Finally, we discuss the seasonal cycle of cirrus clouds' optical and geometrical properties. Figure 6a depicts monthly cirrus cloud frequency (blue line) and daily mean precipitation (green line), with shaded regions indicating the standard deviation of the mean. Cirrus occurrence is lowest during the dry season and highest during the wet and transition seasons, with notable peaks in March and October. Although precipitation peaks in March, the cirrus frequency remains above 70% for much of the year. These maxima coincide with an increased presence of thin and opaque cirrus (Figure 6b). In contrast, SVC maintains an almost constant frequency. Table 2 reports the frequency of occurrence for each cirrus type over the full record and by seasons.

Figure 6c shows how cirrus occurrence frequency varies with altitude in a two-dimensional histogram. The sum of frequencies across altitudes in each month matches that month's overall occurrence, and the dotted white line marks the seasonal tropopause height. The tropopause reaches its minimum (about 16.1 km) during the dry season and its maximum (about 16.7 km) in the wet season. Because thermal inversions at the tropopause inhibit cloud

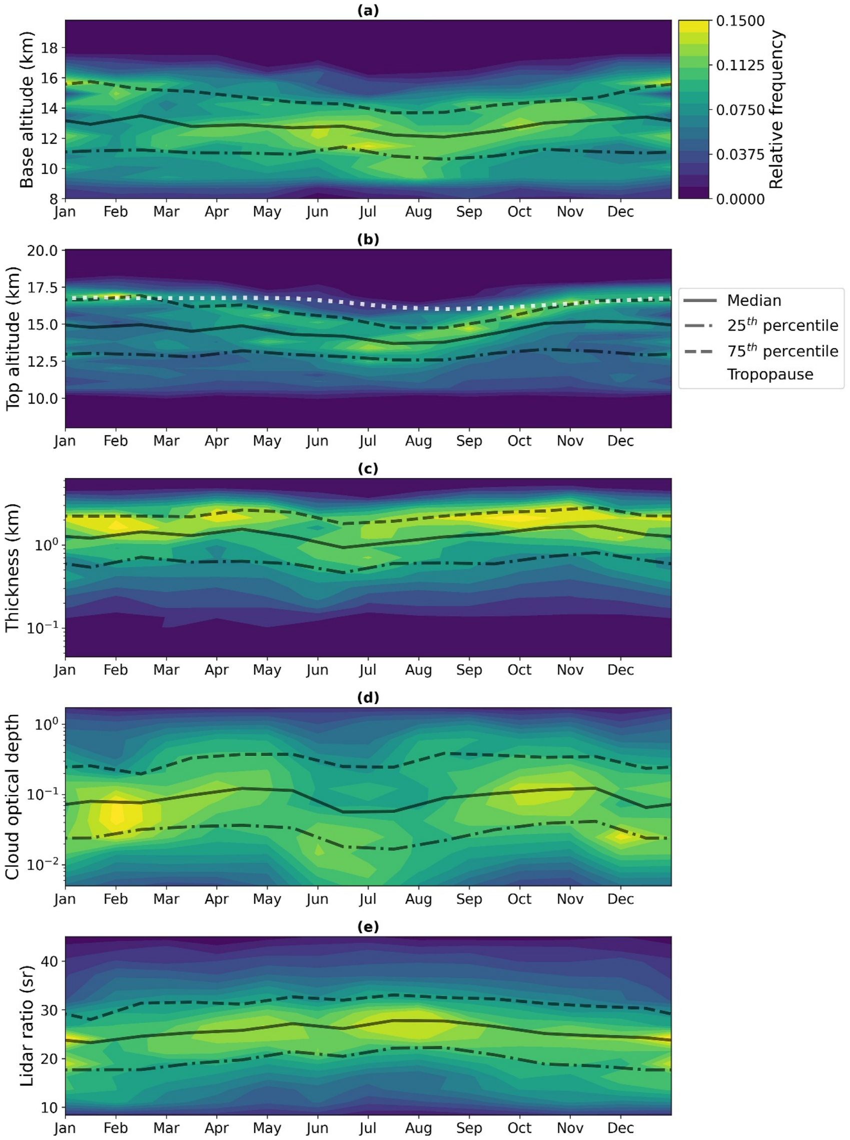

Figure 7. Seasonal cycles of the distribution of (a) base altitude, (b) top altitude, (c) geometric thickness, (d) LR, and (e) COD. The median values, as well as the 25th and 75th percentiles, are also displayed for each property. The white dotted curve represents the tropopause height.

formation in the lower stratosphere, cirrus cloud tops tend to align with seasonal changes in tropopause altitude. Consequently, cirrus clouds are less likely to be found at higher altitudes during the dry season than during the wet season. When cirrus frequency peaks due to a higher occurrence of both thin cirrus (March, April, October, and November), most clouds are concentrated between 12.5 and 15.5 km. Cirrus clouds are present in the stratosphere year-round, though they are much less frequent during the dry season.

We constructed two-dimensional histograms to investigate the seasonal variation of cirrus optical and geometric properties (see Figure 7). The tropopause altitude is displayed in white in the top-altitude plot. The black lines indicate the 25th, 50th (median), and 75th percentiles of the property shown in each panel.

The seasonal variability of cirrus top and base heights is more pronounced in the 75th percentile and median than the 25th percentile. Notably, the 75th percentile of the cloud base height exhibits a more substantial seasonal variation than the cloud top height. When the cirrus top reaches the tropopause—particularly in January and December—it remains nearly constant, whereas the base continues to rise. The median follows a similar seasonal pattern for base and top heights, whereas the 25th percentile presents minimal variation throughout the year.

Cirrus thickness and COD peak in March and October, coinciding with an increased occurrence of opaque and thin cirrus. In contrast, the LR is highest during the dry season, coinciding with a reduced presence of thin cirrus clouds, which have lower LR than opaque cirrus. This shift results in an overall increase in the mean LR. All thickness, COD, and LR percentiles exhibit the same seasonal pattern.

4. Discussion

4.1. Optical and Geometric Properties

In our multiyear ground-based lidar study (July 2011–December 2017), cirrus clouds were detected in more than two-thirds of the measured profiles, presenting substantial seasonal and diurnal variations. During the wet season, cirrus frequency peaked in tandem with higher top altitudes and greater geometric thickness. In contrast, the dry season featured reduced cirrus coverage, lower altitudes, and smaller thickness. Furthermore, SVC and thin cirrus systematically resided at higher altitudes than opaque cirrus, often near the tropopause.

Our estimated cirrus occurrence frequencies for the wet (81.8%) and dry (56.7%) seasons are lower than those reported by Gouveia et al. (2017) (88.1% and 58.2%, respectively). One plausible explanation for this discrepancy is that the single year analyzed by Gouveia et al. (2017) (2011/2012) featured higher and more consistent precipitation rates (10.1 ± 0.4 mm/day) than the multiyear average examined here (9.3 ± 2.0 mm/day). Another contributing factor and important difference to the previous study of Gouveia et al. (2017) was the use of a minimum threshold for the COD values of cirrus layers. This was imposed to reduce day/night sampling biases present in Gouveia's study, but it will inadvertently reduce the detection of SVC clouds and overall cirrus frequency.

This study's average cirrus base height was 12.8 ± 2.2 km, top height was 14.4 ± 1.9 km, and the geometric thickness was 1.61 ± 1.17 km. These properties exhibited statistically significant seasonality, reaching maximum values in the wet and transition seasons and minimum values in the dry season. These results are consistent with the findings of Gouveia et al. (2017) at the same site, where similar altitudes and thicknesses were reported based on a shorter data set. Regional comparisons reinforce this consistency: for example, Seifert et al. (2007) in Hulhule, Maldives and Pandit et al. (2015) in Gadanki, India, reported mean base and top altitudes that fall within a similar range. Differences in base and top altitudes between our study and by Portella and Barbosa (2024) (13.2 ± 2.1 km and 15.4 ± 2.2 km, respectively) using CALIPSO data over the Amazon reflect methodological differences. While polar-orbiting satellites only observe the clouds, ground-based lidars observe the whole diurnal cycle. As shown, there is an evident diurnal cycle for all geometrical and optical properties of cirrus clouds; hence, the ground-based average should correspond more closely to reality.

Nonetheless, the broad agreement across tropical regions suggests a robust climatological pattern of high cirrus layers, as opposed to midlatitudes, where cirrus clouds tend to form a few kilometers lower on average. These trends are further supported by the values compiled in Table 3, which summarizes cirrus cloud properties from various studies across different latitudes. The table highlights that tropical cirrus generally form at higher altitudes than midlatitude and polar regions, reinforcing the observed climatological pattern in our study. This distribution aligns with the dependence of cirrus cloud geometric properties on tropopause height and regional convective activity, which play key roles in governing their formation and vertical extent in tropical regions.

Breaking down geometric properties by cirrus categories also clarifies vertical separation: SVC and thin cirrus typically appeared at higher altitudes than opaque cirrus clouds. This result echoes the 1-year study by Gouveia et al. (2017), which showed differences of less than 300 m between base and top altitudes across similar cirrus classes.

An average LR of 26.1 ± 8.3 sr (corrected for multiple scattering) was derived for cirrus in this study, closely aligning with the typical literature values of approximately 25 sr (see Table 3). Similarly, the observed COD of 0.27 ± 0.40 is close to the COD = 0.25 ± 0.46 reported by Gouveia et al. (2017). Seasonal variations in LR could stem from changes in ice crystal habits (e.g., plates vs. columns) and from aerosol concentrations that act as ice-nucleating particles during the wet versus dry seasons. Sassen et al. (1989) also noted that different ice crystal types—thin plate or long column in opaque cirrus versus thick plate in thinner cirrus—can alter the backscatter signal and thus the inferred LR. Panel (f) of Figure 2 indicates potential shifts in ice crystal habit across cirrus subcategories. Opaque cirrus' association with thin plate and long column crystals, versus higher thick plate

Table 3
Properties of Cirrus Clouds in the Literature Sorted by the Latitude of the Experimental Site

			Altitude (km)			Frequency (%)		
Experimental site	Study period	λ (nm)	Base	Top	Thickness	SVC	Thin	LR (sr)
Ny-Ålesund, Svalbard 78.9°N, 11.9°E	2011–2020 Nakoudi et al. (2021)	355	7.1	9.5				33
Kuopio, Finland 62.74°N, 27.54°E	2008–2016 Voudouri et al. (2020)	355	8.60	9.80	1.20	3	71	33
Salt Lake City, Utah, USA* 49.8°N, 111.8°W	1986–1996 Sassen and Comstock (2001)	694	8.8	11.2	1.8	50		
Haute-Provence, France* 43.9°N, 5.7°E	1997–2007 Hoareau et al. (2013)	532/1,064	9.3	10.7	1.4	38		18.2
Thessaloniki, Greece* 40.6°N, 22.9°E	2000–2006 Giannakaki et al. (2007)	355/532	8.6	11.7	2.7		57	30
Seoul, South Korea* 37°N, 127°E	2006–2009 Kim et al. (2014)	532/1,064	8.8	10.6				20
Buenos Aires, Argentina* 34.6°S, 58.5°W	2001–2005 Lakkis et al. (2009)	532	9.6	11.8	2.4			
Nagu, Tibet 31.48°S, 96.02°E	July–August 2014 Dai et al. (2019)	532	7.46	8.41	1.22	4.76	61.90	
Wuhan, China 30.5°N 114.3°E	2019–2020 W. Wang et al. (2020)	532	10.2	12.7	2.5	18	51	21.6
Gwal Pahari, India 28.43°N, 77.15°E	2008–2016 Voudouri et al. (2020)	355	9.00	10.60	1.50	0	20	27
Elandsfotein, South Africa 25.25°S, 29.43°E	2008–2016 Voudouri et al. (2020)	355	9.20	10.836	1.60	2	61	26
Camagüey, Cuba* 21.4°N, 77.9°W	1993–1998 Marrero and Barja (2006)	532	11.6	13.8		25		
Reúnion, France* 21°S, 55°E	1996–2001 Cadet (2003)	532	11	14		65		18.3†
Gadanki, India* 13.5°N, 79.2°E	1998–2013 Pandit et al. (2015)	532	13.0	15.3	2.3	52	36	
Hulhule, Maldives* 4.1°N, 73.3°E	1999–2000 Seifert et al. (2007)	532	11.9	13.7	1.8	15	49	32
Mahé, Seychelles* 4.4°S, 55.3°E	February–March 1999 Pace (2003)	532			0.2–2			19†
Amazon rainforest, Brazil 2.89°S, 59.97°W	July 2011–June 2012 Gouveia et al. (2017)	355	12.7	14.4	1.7	41.6	37.8	23.3
Nauru 0.5°S, 166.9°E	April–November 1999 Comstock et al. (2002)	532	~14	~16				

Note. The horizontal bands separate the polar regions, midlatitudes, and tropics. The papers marked with * are discussed in Gouveia et al. (2017), and the LR marked with † have not been corrected for multiple scattering. Altered from Gouveia et al. (2017).

fractions in thin/SVC clouds, suggests that cloud microphysics interact with vertical motion and supersaturation levels differently for each cirrus type.

4.2. Diurnal Cycle

Our 7-year lidar record confirms a pronounced diurnal cycle in Amazonian cirrus. Cloud cover reaches its minimum near local noon, rises rapidly through the late afternoon, peaks just after sunset, and decreases again after midnight. The amplitude is greatest for opaque cirrus, whereas thin and SVC layers fluctuate more modestly. The diurnal cycle of the occurrence of cirrus clouds identified in this study agrees with the findings of Gouveia et al. (2017). By expanding the 1-year data set to 5,481 hr of observations, the extended record narrows statistical uncertainties and yields a firmer characterization of the diurnal signal.

Feofilov and Stubenrauch (2019), combining AIRS and IASI, retrieved a similar land-based pattern for tropical high-level clouds: a minimum around 12:00 LT, rapid growth during the afternoon, a maximum during the evening–night period, and decay toward dawn. In our Amazonian record, the buildup is similar, but the peak arrives about 3 hours before the satellite product indicates. This difference is expected: the global product averages 1° × 1° pixels and only four local times, whereas our ground lidar resolves the fast local evolution above an active convective hotspot. Feofilov and Stubenrauch also reported a gradual thickening of cirrus from late afternoon into the night, a trend we confirm.

Thorsen et al. (2013) compared CALIOP with colocated micropulse and Raman lidars at Darwin (Australia) and attributed the observed daytime drop in cirrus frequency and daytime thinning of cirrus clouds to solar background noise contaminating the micropulse data. We mitigate this bias by applying a minimum threshold for COD (0.005), which helps ensure more consistent detection during both day and night. Moreover, our conditional sampling accounts for the different samplings throughout the day or seasons. Finally, the fact that we observe coherent diurnal changes in frequency and precipitation, in line with satellite studies (Feofilov & Stubenrauch, 2019), suggests that our signal is physical rather than instrumental.

Nonetheless, biases in geometric and optical properties persist because they are more difficult to correct for. Moreover, these biases depend on how the analysis is performed. For instance, Figure 4a shows the diurnal cycle of cloud base height for each season. Since the data are segregated by hours and seasons, there are no significant differences in sampling; hence there are no biases. On the other hand, Figure 5a shows the same but segregated by cirrus categories. Since each curve includes data from different seasons, the averages are biased toward the dry season, which has more data than the wet season. Similarly, the seasonal cycles of cloud base height in Figure 7a are biased toward the nighttime, which has more data than the daytime period. These limitations, inherent to any ground-based lidar observations of high clouds, must be taken into account when interpreting the diurnal cycle. An alternative method that future studies could consider is resampling the observations according to the frequency of occurrence. This would produce a pseudo-data set of cirrus properties that is sampling-corrected and uniformly distributed.

Model experiments at a semiarid midlatitude site showed that neglecting the cirrus diurnal cycle can bias daily mean top-of-atmosphere (TOA) net fluxes by up to 11 $\mathrm{Wm^{-2}}$ (M. Wang et al., 2022). Cirrus clouds over Amazonia are more frequent, optically thicker, and display a larger afternoon-to-night contrast than at that site (Feofilov & Stubenrauch, 2019). Because COD controls both solar reflection and infrared trapping, the stronger cycle documented here should translate into even larger TOA biases in tropical regions. Similarly, estimating the radiative forcing of cirrus clouds based on polar-orbiting satellites, which measure only twice per day, can also introduce significant bias (Gouveia, 2018).

4.3. Mechanism of Formation of Cirrus Clouds

Deep convection is the principal driver of cirrus cloud formation in the Amazon (Gouveia et al., 2017), through the detachment of an anvil from the upper portion of cumulonimbus towers. During the wet season, the tropopause altitude averages around 16.77 ± 0.11 km, whereas in the dry season, it lowers to 16.13 ± 0.13 km. Because the anvil stops developing vertically when it encounters the tropopause, the maximum altitude at which cirrus clouds form also follows this seasonal shift. In especially intense convective events, the cloud tops can overshoot the tropopause—known as overshooting tops (Liu & Zipser, 2005)—producing cirrus layers that extend into the lower stratosphere. Our observations confirm that most cirrus clouds remain below the tropopause, though a fraction extends above it: 4.0% of cirrus bases were located in the stratosphere, and 15.4% had tops above the tropopause. These values closely match those of Gouveia et al. (2017), who found 5.9% and 15.7%, respectively.

Freshly formed opaque cirrus appear at altitudes comparable to the parent convective cloud tops. Figures 2a and 2b indicate that these new, thicker clouds tend to be located well below the tropopause (on average, about 6.5 km below) and exhibit larger COD. Over time, advection and dispersion by upper-level winds spread the ice crystals out. As they drift away from the convective core and undergo lifting, the clouds become thinner both geometrically and optically due to vertical wind shear (Jensen et al., 1996). Consequently, thin cirrus and SVC are more commonly observed closer to the tropopause.

This cloud formation and transformation process is further modulated by the diurnal cycle, which is tightly linked to the progression of convective activity peaking in the late afternoon, which peaks around 16 LT during the dry season and 14 LT in the wet season. As convective towers intensify, new anvils form and detach, producing fresh opaque cirrus clouds. The onset of these clouds is accompanied by an increase in cirrus thickness and COD, coupled with a decrease in base and top altitudes. These detached anvils drift throughout the night, gradually thinning, rising, and partially evaporating. Thus, by dawn, cirrus layers often appear closer to the tropopause, thinner, with lower COD.

Overall, this convective detachment process, combined with the seasonal variability of the tropopause height and the day-night differences in convective vigor, governs where and when cirrus clouds form, how they ascend to the tropopause, and how they become thinner with time. Shifts in convective intensity, including nocturnal mesoscale convective complexes (Burleyson et al., 2016), can still generate new cirrus layers overnight, particularly during the wet season. This phenomenon may explain sporadic early morning increases in cirrus COD, as well as temporary decreases in their base and top altitudes during the wet season when late night or predawn convection intensifies.

In summary, the detachment of the convective anvil near or slightly above the tropopause remains the dominant mechanism for cirrus formation in this region. Subsequent processes, such as cloud top lifting and ice crystal evolution, lead to thinner cirrus types that persist at higher altitudes, and occasionally in the stratosphere, until they eventually disperse or evaporate.

5. Conclusions

This study analyzed 5,481 hr of lidar measurements collected between July 2011 and December 2017 in the central Amazon region. By applying an automated cirrus cloud detection algorithm, we identified the base height, top height, and geometric thickness of cirrus clouds, as well as their COD and LR. On average, cloud base altitude, top altitude, geometric thickness, and COD were 12.8 ± 2.2 km, 14.4 ± 1.9 km, 1.61 ± 1.17 km, and 0.27 ± 0.40, respectively. Furthermore, thin and SVC cirrus clouds were observed to have base and top heights closer to the tropopause than opaque cirrus. When comparing these results with previous studies, a high degree of consistency was observed, with similar patterns reported by other researchers in tropical regions. The mean LR obtained in this study was 26.1 ± 8.3 sr, which agrees with values reported in the literature that also applied multiple scattering corrections.

This work provides the first detailed assessment of the diurnal cycle of cirrus clouds in the Amazon region. Cirrus formation predominantly peaks from late afternoon into the overnight hours, especially during the wet season, mirroring heightened convective activity. In parallel with this increase, newly formed cirrus layers tend to be geometrically thicker and optically denser earlier in the afternoon. As the day progresses, these layers gradually become thinner and ascend toward the tropopause, leading to thin and SVC cirrus by late evening and early morning. Because neglecting this diurnal variability can introduce sizable errors into estimates of cloud radiative effects, the hourly view of optical and geometrical properties reported here should serve as a valuable reference for models that aim to represent the radiative influence of Amazonian cirrus.

Seasonally, cirrus occurrence was highest during the wet season (81.8%) compared to the dry season (56.7%), with thin cirrus layers being most common (48.4%), followed by opaque (26.4%) and SVC (25.2%). Cirrus clouds were also thicker and at higher altitudes during the wet season, accompanied by a greater frequency of opaque cirrus layers (26.8%) and a mean top height of 14.7 km, while dry season cirrus featured fewer opaque layers (13.9%) and a lower average top height of 13.9 km. LR similarly varied: higher values were observed during the dry season (27.1 sr) than the wet season (25.3 sr), and opaque cirrus featured higher ratios (28.8 sr) than thin (24.7 sr) or SVC (22.2 sr), hinting at distinct ice crystal morphologies across cirrus types. Notably, cloud top height showed more pronounced seasonality than cloud base height—particularly for the 75% and 50% percentiles—likely reflecting seasonal changes in the tropopause altitude.

Although our observations are extensive, this single-site study may not fully represent other parts of the Amazon. Still, the high temporal resolution of ground-based lidar measurements offers a clear advantage for capturing diurnal cycles of cirrus properties, serving as a valuable benchmark for both satellite-based analyses and numerical modeling of the atmosphere. Additionally, although our results qualitatively suggest that cirrus clouds originate from deep convective processes, we did not quantitatively link observed cirrus layers to active convection. Future research could address this gap by employing HYSPLIT back trajectories to trace cirrus clouds back to their parent cumulonimbus. This would likely reveal distinct temporal distributions among different cirrus types—opaque cirrus likely younger than thinner, SVC cirrus—and strengthen our understanding of cirrus formation pathways. Furthermore, expanding the lidar network, integrating satellite data, and studying mesoscale convective complexes in the nocturnal wet season are promising routes to refine and extend the conclusions drawn here.

Conflict of Interest

The authors declare no conflicts of interest relevant to this study.

Data Availability Statement

The algorithm used to process the cirrus data is openly available at a Zenodo repository (Cordeiro, 2025), along with a file containing all geometrical and optical properties of the retrieved cirrus layers (https://doi.org/10.5281/zenodo.17064548). Additional public domain data sets were also used. The radiosonde profiles were accessed through the University of Wyoming repository (https://weather.uwyo.edu/upperair/sounding.shtml). The CMORPH precipitation data set (Xie et al., 2019) is distributed by the NOAA Climate Prediction Center (https://doi.org/10.25921/w9va-q159). Tropopause heights were obtained from the AIRS Level 3 Monthly Gridded Retrieval Product AIRS3STD V7 (AIRS Project, 2019), available from NASA's GES DISC archive (https://doi.org/10.5067/UO3Q64CTTS1U).

Acknowledgments

LPC acknowledges the support by the Coordenação de Aperfeiçoamento de Pessoal de Nível Superior—Brasil (CAPES)—Finance Code 001. HMJB acknowledges the financial support from FAPESP under research Grant 2013/50510-5. We thank Martina Krämer for sharing the aircraft data on tropical cirrus. We thank EMBRAPA and the Brazilian Institute for Research in Amazonia for logistical support at the experimental site. Special thanks go to Marcelo Rossi, Victor Souza, and Jocivaldo Souza at Embrapa and to Ruth Araujo, Roberta Souza, Bruno Takeshi, and Glauber Cirino from INPA. The Article Processing Charge for the publication of this research was funded by the Coordenação de Aperfeiçoamento de Pessoal de Nível Superior - Brasil (CAPES) (ROR identifier: 00x0ma614).

References

AIRS Project. (2019). Aqua/AIRS L3 daily standard physical retrieval (AIRS-only) 1 degree x 1 degree V7.0 [Dataset]. *Goddard Earth Sciences Data and Information Services Center (GES DISC)*. Greenbelt, MD, USA. https://doi.org/10.5067/UO3Q64CTTS1U

Atlas, R. L., Bretherton, C. S., Sokol, A. B., Blossey, P. N., & Khairoutdinov, M. F. (2024). Tropical cirrus are highly sensitive to ice microphysics within a nudged global storm-resolving model. *Geophysical Research Letters*, *51*(1), e2023GL105868. https://doi.org/10.1029/2023GL105868

Barbosa, H. M. J., Barja, B., Pauliquevis, T., Gouveia, D. A., Artaxo, P., Cirino, G. G., et al. (2014). A permanent Raman lidar station in the Amazon: Description, characterization, and first results. *Atmospheric Measurement Techniques*, *7*(6), 1745–1762. https://doi.org/10.5194/amt-7-1745-2014

Burleyson, C. D., Feng, Z., Hagos, S. M., Fast, J., Machado, L. A. T., & Martin, S. T. (2016). Spatial variability of the background diurnal cycle of deep convection around the goamazon2014/5 field campaign sites. *Journal of Applied Meteorology and Climatology*, *55*(7), 1579–1598. https://doi.org/10.1175/JAMC-D-15-0229.1

Cadet, B., Goldfarb, L., Faduilhe, D., Baldy, S., Giraud, V., Keckhut, P., & Réchou, A. (2003). A sub-tropical cirrus clouds climatology from Reunion Island (21°S, 55°E) lidar data set. *Geophysical Research Letters*, *30*(3), 2002GL016342. https://doi.org/10.1029/2002gl016342

Campbell, J. R., Vaughan, M. A., Oo, M., Holz, R. E., Lewis, J. R., & Welton, E. J. (2015). Distinguishing cirrus cloud presence in autonomous lidar measurements. *Atmospheric Measurement Techniques*, *8*(1), 435–449. https://doi.org/10.5194/amt-8-435-2015

Comstock, J. M., Ackerman, T. P., & Mace, G. G. (2002). Ground-based lidar and radar remote sensing of tropical cirrus clouds at Nauru Island: Cloud statistics and radiative impacts. *Journal of Geophysical Research*, *107*(D23), 4714. https://doi.org/10.1029/2002jd002203

Cordeiro, L. (2025). Algorithm for processing cirrus data and dataset of retrieved properties. [collection]. *Zenodo*. https://doi.org/10.5281/zenodo.17064548

Dai, G., Wu, S., Song, X., & Liu, L. (2019). Optical and geometrical properties of cirrus clouds over the Tibetan plateau measured by lidar and radiosonde sounding during the summertime in 2014. *Remote Sensing*, *11*(3), 302. https://doi.org/10.3390/rs11030302

Feofilov, A. G., & Stubenrauch, C. J. (2019). Diurnal variation of high-level clouds from the synergy of AIRS and IASI space-borne infrared sounders. *Atmospheric Chemistry and Physics*, *19*(22), 13957–13972. https://doi.org/10.5194/acp-19-13957-2019

Gasparini, B., & Lohmann, U. (2016). Why cirrus cloud seeding cannot substantially cool the planet. *Journal of Geophysical Research: Atmospheres*, *121*(9), 4877–4893. https://doi.org/10.1002/2015jd024666

Gasparini, B., Sullivan, S. C., Sokol, A. B., Kärcher, B., Jensen, E., & Hartmann, D. L. (2023). Opinion: Tropical cirrus – From micro-scale processes to climate-scale impacts. *Atmospheric Chemistry and Physics*, *23*(24), 15413–15444. https://doi.org/10.5194/acp-23-15413-2023

Giannakaki, E., Balis, D. S., Amiridis, V., & Kazadzis, S. (2007). Optical and geometrical characteristics of cirrus clouds over a southern European lidar station. *Atmospheric Chemistry and Physics*, *7*(21), 5519–5530. https://doi.org/10.5194/acp-7-5519-2007

Gouveia, D. A. (2018). *Forçante radiativa, propriedades ópticas e físicas das nuvens cirrus na amazônia*. Doctoral dissertation. Universidade de São Paulo. São Paulo, SP. https://doi.org/10.11606/T.43.2019.tde-08022019-141530

Gouveia, D. A., Barbosa, H. M. J., & Barja, B. (2014). Characterization of cirrus clouds in central amazon (2.89°S, 59.97°W): Firsts results from observations in 2011. *Optica Pura y Aplicada*, *47*(2), 109–114. https://doi.org/10.7149/OPA.47.2.109

Gouveia, D. A., Barja, B., Barbosa, H. M. J., Seifert, P., Baars, H., Pauliquevis, T., & Artaxo, P. (2017). Optical and geometrical properties of cirrus clouds in Amazonia derived from 1 year of ground-based lidar measurements. *Atmospheric Chemistry and Physics*, *17*(5), 3619–3636. https://doi.org/10.5194/acp-17-3619-2017

Haladay, T., & Stephens, G. (2009). Characteristics of tropical thin cirrus clouds deduced from joint CloudSat and CALIPSO observations. *Journal of Geophysical Research*, *114*(D8), 2008JD010675. https://doi.org/10.1029/2008jd010675

Heymsfield, A. J., Krämer, M., Luebke, A., Brown, P., Cziczo, D. J., Franklin, C., et al. (2017). Cirrus clouds. *Meteorological Monographs*, *58*(2), 1–2.26. https://doi.org/10.1175/amsmonographs-d-16-0010.1

Hoareau, C., Keckhut, P., Noel, V., Chepfer, H., & Baray, J.-L. (2013). A decadal cirrus clouds climatology from ground-based and spaceborne lidars above the south of France (43.9° N–5.7° E). *Atmospheric Chemistry and Physics*, *13*(14), 6951–6963. https://doi.org/10.5194/acp-13-6951-2013

Hogan, R. J. (2008). Fast lidar and radar multiple-scattering models. Part I: Small-angle scattering using the photon variance–covariance method. *Journal of the Atmospheric Sciences*, *65*(12), 3621–3635. https://doi.org/10.1175/2008JAS2642.1

Horner, G., & Gryspeerdt, E. (2025). How does the lifetime of detrained cirrus impact the high-cloud radiative effect in the tropics? *Atmospheric Chemistry and Physics*, *25*(11), 5617–5631. https://doi.org/10.5194/acp-25-5617-2025

Jeggle, K., Neubauer, D., Binder, H., & Lohmann, U. (2025). Cirrus formation regimes – Data-driven identification and quantification of mineral dust effect. *Atmospheric Chemistry and Physics*, *25*(13), 7227–7243. https://doi.org/10.5194/acp-25-7227-2025

Jensen, E. J., Kärcher, B., Woods, S., Krämer, M., & Ueyama, R. (2024). The impact of gravity waves on the evolution of tropical anvil cirrus microphysical properties. *Journal of Geophysical Research: Atmospheres*, *129*(5), e2023JD039887. https://doi.org/10.1029/2023JD039887

Jensen, E. J., Toon, O. B., Selkirk, H. B., Spinhirne, J. D., & Schoeberl, M. R. (1996). On the formation and persistence of subvisible cirrus clouds near the tropical tropopause. *Journal of Geophysical Research*, *101*(D16), 21361–21375. https://doi.org/10.1029/95jd03575

Kärcher, B., DeMott, P. J., Jensen, E. J., & Harrington, J. Y. (2022). Studies on the competition between homogeneous and heterogeneous ice nucleation in cirrus formation. *Journal of Geophysical Research: Atmospheres*, *127*(3), e2021JD035805. https://doi.org/10.1029/2021JD035805

Kim, Y., Kim, S.-W., Kim, M.-H., & Yoon, S.-C. (2014). Geometric and optical properties of cirrus clouds inferred from three-year ground-based lidar and CALIOP measurements over Seoul, Korea. *Atmospheric Research*, *139*, 27–35. https://doi.org/10.1016/j.atmosres.2013.12.016

King, M. D., Platnick, S., Menzel, W. P., Ackerman, S. A., & Hubanks, P. A. (2013). Spatial and temporal distribution of clouds observed by MODIS onboard the Terra and Aqua satellites. *IEEE Transactions on Geoscience and Remote Sensing*, *51*(7), 3826–3852. https://doi.org/10.1109/tgrs.2012.2227333

Klett, J. D. (1985). Lidar inversion with variable backscatter/extinction ratios. *Applied Optics*, *24*(11), 1638. https://doi.org/10.1364/ao.24.001638

Krämer, M., Rolf, C., Luebke, A., Afchine, A., Spelten, N., Costa, A., et al. (2016). A microphysics guide to cirrus clouds – Part 1: Cirrus types. *Atmospheric Chemistry and Physics*, *16*(5), 3463–3483. https://doi.org/10.5194/acp-16-3463-2016

Krisna, T. C., Wendisch, M., Ehrlich, A., Jäkel, E., Werner, F., Weigel, R., et al. (2018). Comparing airborne and satellite retrievals of cloud optical thickness and particle effective radius using a spectral radiance ratio technique: Two case studies for cirrus and deep convective clouds. *Atmospheric Chemistry and Physics*, *18*(7), 4439–4462. https://doi.org/10.5194/acp-18-4439-2018

Lakkis, S. G., Lavorato, M., & Canziani, P. O. (2009). Monitoring cirrus clouds with lidar in the southern hemisphere: A local study over Buenos Aires. 1. Tropopause heights. *Atmospheric Research*, *92*(1), 18–26. https://doi.org/10.1016/j.atmosres.2008.08.003

Lin, L., Liu, X., Zhao, X., Shan, Y., Ke, Z., Lyu, K., & Bowman, K. P. (2025). Ice nucleation by volcanic ash greatly alters cirrus cloud properties. *Science Advances*, *11*(19), eads0572. https://doi.org/10.1126/sciadv.ads0572

Liou, K.-N. (1986). Influence of cirrus clouds on weather and climate processes: A global perspective. *Monthly Weather Review*, *114*(6), 1167–1199. https://doi.org/10.1175/1520-0493(1986)114<1167:ioccow>2.0.co;2

Liu, C., & Zipser, E. J. (2005). Global distribution of convection penetrating the tropical tropopause. *Journal of Geophysical Research*, *110*(D23), 2005JD006063. https://doi.org/10.1029/2005jd006063

Lohmann, U., Lüönd, F., & Mahrt, F. (2016). *An introduction to clouds*. Cambridge University Press. https://doi.org/10.1017/CBO9781139087513

Luebke, A. E., Avallone, L. M., Schiller, C., Meyer, J., Rolf, C., & Krämer, M. (2013). Ice water content of arctic, midlatitude, and tropical cirrus – Part 2: Extension of the database and new statistical analysis. *Atmospheric Chemistry and Physics*, *13*(13), 6447–6459. https://doi.org/10.5194/acp-13-6447-2013

Luo, Y., Krueger, S. K., & Moorthi, S. (2005). Cloud properties simulated by a single-column model. Part I: Comparison to cloud radar observations of cirrus clouds. *Journal of the Atmospheric Sciences*, *62*(5), 1428–1445. https://doi.org/10.1175/JAS3425.1

Lynch, D. K., Sassen, K., Starr, D. O., & Stephens, G. (2002). *Cirrus*. Oxford University Press. https://doi.org/10.1093/oso/9780195130720.001.0001

Mace, G. G., Benson, S., & Kato, S. (2006). Cloud radiative forcing at the atmospheric radiation measurement program climate research facility: 2. Vertical redistribution of radiant energy by clouds. *Journal of Geophysical Research*, *111*(D11), 2005JD005922. https://doi.org/10.1029/2005jd005922

Machado, L. A. T., Dias, M. A. F. S., Morales, C., Fisch, G., Vila, D., Albrecht, R., et al. (2014). The chuva project: How does convection vary across Brazil? *Bulletin of the American Meteorological Society*, *95*(9), 1365–1380. https://doi.org/10.1175/BAMS-D-13-00084.1

Marrero, J. C. A., & Barja, B. (2006). Cirrus clouds optical properties measured with lidar at Camagüey, Cuba. *Optica Pura y Aplicada*, *39*, 11–16.

Martin, S. T., Artaxo, P., Machado, L. A. T., Manzi, A. O., Souza, R. A. F., Schumacher, C., et al. (2016). Introduction: Observations and modeling of the green ocean Amazon (goamazon2014/5). *Atmospheric Chemistry and Physics*, *16*(8), 4785–4797. https://doi.org/10.5194/acp-16-4785-2016

McFarquhar, G. M., Heymsfield, A. J., Spinhirne, J., & Hart, B. (2000). Thin and subvisual tropopause tropical cirrus: Observations and radiative impacts. *Journal of the Atmospheric Sciences*, *57*(12), 1841–1853. https://doi.org/10.1175/1520-0469(2000)057⟨1841:tasttc⟩2.0.co;2

Nakoudi, K., Stachlewska, I. S., & Ritter, C. (2021). An extended lidar-based cirrus cloud retrieval scheme: First application over an arctic site. *Optics Express*, *29*(6), 8553. https://doi.org/10.1364/oe.414770

Pace, G., Cacciani, M., di Sarra, A., Fiocco, G., & Fuà, D. (2003). Lidar observations of equatorial cirrus clouds at Mahé Seychelles. *Journal of Geophysical Research*, *108*(D8), 2002JD002710. https://doi.org/10.1029/2002jd002710

Pandit, A. K., Gadhavi, H. S., Venkat Ratnam, M., Raghunath, K., Rao, S. V. B., & Jayaraman, A. (2015). Long-term trend analysis and climatology of tropical cirrus clouds using 16 years of lidar data set over southern India. *Atmospheric Chemistry and Physics*, *15*(24), 13833–13848. https://doi.org/10.5194/acp-15-13833-2015

Portella, B. M., & Barbosa, H. M. J. (2024). Climatology and trends of cirrus geometrical and optical properties in the Amazon region from 7-yr of calipso observations. *Atmospheric Research*, *299*, 107167. https://doi.org/10.1016/j.atmosres.2023.107167

Potter, B. E., & Holton, J. R. (1995). The role of monsoon convection in the dehydration of the lower tropical stratosphere. *Journal of the Atmospheric Sciences*, *52*(8), 1034–1050. https://doi.org/10.1175/1520-0469(1995)052⟨1034:TROMCI⟩2.0.CO;2

Protat, A., Young, S. A., McFarlane, S. A., L'Ecuyer, T., Mace, G. G., Comstock, J. M., et al. (2014). Reconciling ground-based and space-based estimates of the frequency of occurrence and radiative effect of clouds around Darwin, Australia. *Journal of Applied Meteorology and Climatology*, *53*(2), 456–478. https://doi.org/10.1175/jamc-d-13-072.1

Sassen, K., & Cho, B. S. (1992). Subvisual-thin cirrus lidar dataset for satellite verification and climatological research. *Journal of Applied Meteorology*, *31*(11), 1275–1285. https://doi.org/10.1175/1520-0450(1992)031<1275:stcldf>2.0.co;2

Sassen, K., & Comstock, J. M. (2001). A midlatitude cirrus cloud climatology from the facility for atmospheric remote sensing. Part III: Radiative properties. *Journal of the Atmospheric Sciences*, *58*(15), 2113–2127. https://doi.org/10.1175/1520-0469(2001)058⟨2113:amcccf⟩2.0.co;2

Sassen, K., Griffin, M. K., & Dodd, G. C. (1989). Optical scattering and microphysical properties of subvisual cirrus clouds, and climatic implications. *Journal of Applied Meteorology*, *28*(2), 91–98. https://doi.org/10.1175/1520-0450(1989)028<0091:osampo>2.0.co;2

Sassen, K., Wang, Z., & Liu, D. (2008). Global distribution of cirrus clouds from CloudSat/Cloud-Aerosol lidar and infrared pathfinder satellite observations (CALIPSO) measurements. *Journal of Geophysical Research*, *113*(D8), 2008JD009972. https://doi.org/10.1029/2008jd009972

Sassen, K., Wang, Z., & Liu, D. (2009). Cirrus clouds and deep convection in the tropics: Insights from CALIPSO and CloudSat. *Journal of Geophysical Research*, *114*(D4), 2009JD011916. https://doi.org/10.1029/2009jd011916

Seifert, P., Ansmann, A., Müller, D., Wandinger, U., Althausen, D., Heymsfield, A. J., et al. (2007). Cirrus optical properties observed with lidar, radiosonde, and satellite over the tropical Indian Ocean during the aerosol-polluted northeast and clean maritime southwest monsoon. *Journal of Geophysical Research*, *112*(D17), 2006JD008352. https://doi.org/10.1029/2006jd008352

Spichtinger, P., & Gierens, K. M. (2009). Modelling of cirrus clouds – Part 1a: Model description and validation. *Atmospheric Chemistry and Physics*, *9*(2), 685–706. https://doi.org/10.5194/acp-9-685-2009

Thorsen, T. J., Fu, Q., & Comstock, J. (2011). Comparison of the calipso satellite and ground-based observations of cirrus clouds at the arm twp sites. *Journal of Geophysical Research*, *116*(D21), D21203. https://doi.org/10.1029/2011jd015970

Thorsen, T. J., Fu, Q., Comstock, J. M., Sivaraman, C., Vaughan, M. A., Winker, D. M., & Turner, D. D. (2013). Macrophysical properties of tropical cirrus clouds from the calipso satellite and from ground-based micropulse and raman lidars. *Journal of Geophysical Research: Atmospheres*, *118*(16), 9209–9220. https://doi.org/10.1002/jgrd.50691

Voudouri, K. A., Giannakaki, E., Komppula, M., & Balis, D. (2020). Variability in cirrus cloud properties using a Polly^{XT} raman lidar over high and tropical latitudes. *Atmospheric Chemistry and Physics*, *20*(7), 4427–4444. https://doi.org/10.5194/acp-20-4427-2020

Wandinger, U. (1998). Multiple-scattering influence on extinction- and backscatter-coefficient measurements with raman and high-spectral-resolution lidars. *Applied Optics*, *37*(3), 417. https://doi.org/10.1364/ao.37.000417

Wang, M., Su, J., Peng, N., Xu, Y., & Ge, J. (2022). Diurnal cycle of cirrus cloud and its associated radiative effects at the sacol site. *Atmospheric Research*, *265*, 105887. https://doi.org/10.1016/j.atmosres.2021.105887

Wang, W., Yi, F., Liu, F., Zhang, Y., Yu, C., & Yin, Z. (2020). Characteristics and seasonal variations of cirrus clouds from polarization lidar observations at a 30°n plain site. *Remote Sensing*, *12*(23), 3998. https://doi.org/10.3390/rs12233998

Wehr, T., Kubota, T., Tzeremes, G., Wallace, K., Nakatsuka, H., Ohno, Y., et al. (2023). The Earthcare mission – Science and system overview. *Atmospheric Measurement Techniques*, *16*(15), 3581–3608. https://doi.org/10.5194/amt-16-3581-2023

Wendisch, M., Pöschl, U., Andreae, M. O., Machado, L. A. T., Albrecht, R., Schlager, H., et al. (2016). Acridicon–chuva campaign: Studying tropical deep convective clouds and precipitation over Amazonia using the new German research aircraft halo. *Bulletin of the American Meteorological Society*, *97*(10), 1885–1908. https://doi.org/10.1175/BAMS-D-14-00255.1

Winker, D. M., Pelon, J., Coakley, J. A., Ackerman, S. A., Charlson, R. J., Colarco, P. R., et al. (2010). The CALIPSO mission: A global 3D view of aerosols and clouds. *Bulletin America Meteorology Social*, *91*(9), 1211–1230. https://doi.org/10.1175/2010BAMS3009.1

Winker, D. M., Vaughan, M. A., Omar, A., Hu, Y., Powell, K. A., Liu, Z., et al. (2009). Overview of the CALIPSO mission and CALIOP data processing algorithms. *Journal of Atmospheric and Oceanic Technology*, *26*(11), 2310–2323. https://doi.org/10.1175/2009JTECHA1281.1

Xie, P., Joyce, R., Wu, S., Yoo, S.-H., Yarosh, Y., Sun, F., & Lin, R. (2017). Reprocessed, bias-corrected CMORPH global high-resolution precipitation estimates from 1998. *Journal of Hydrometeorology*, *18*(6), 1617–1641. https://doi.org/10.1175/JHM-D-16-0168.1

Xie, P., Joyce, R., Wu, S., Yoo, S.-H., Yarosh, Y., Sun, F., et al. (2019). NOAA climate data record (CDR) of CPC morphing technique (CMORPH) high resolution global precipitation estimates, version 1 [Dataset]. *NOAA National Centers for Environmental Information*. https://doi.org/10.25921/w9va-q159

Young, S. A. (1995). Analysis of lidar backscatter profiles in optically thin clouds. *Applied Optics*, *34*(30), 7019. https://doi.org/10.1364/ao.34.007019